Adaptive Multi-Band Negative-Group-Delay RF Circuits With Low Reflection

Roberto Gómez-García, *Senior Member, IEEE*, José-María Muñoz-Ferreras, *Member, IEEE*, and Dimitra Psychogiou, *Senior Member, IEEE*

***Abstract*— Two classes of frequency-reconfigurable multi-band negative-group-delay (NGD) circuit networks that feature low-input-power-reflection capabilities are reported. They consist of lossy-complementary-diplexer architectures, in which the NGD properties are obtained within the stopband regions of their lossy multi-band bandstop-filter (BSF) channel. Their complementary lossy multi-band bandpass-filter (BPF) branch absorbs in its terminating resistor the RF-input-signal energy that is not transmitted by the lossy multi-band BSF channel within its stopbands. In this manner, the input-reflectionless/absorptive behavior is realized. The theoretical foundations of the devised lossy-multi-band-BSF-based NGD structures using a coupling-routing-diagram formalism and single-to-multi-band admittance transformations are described. For the first-order case as illustration, guidelines for the synthesis in the bandpass frequency domain are provided. Furthermore, the extension of these multi-band NGD approaches to higher-order and in-series-cascade multi-stage realizations for more-general and wider-band NGD patterning, as well as to two-port/symmetrical designs, is shown. In addition, the conception of multi-functional passive components with NGD characteristics, such as wide-band BPFs and power directional couplers with embedded NGD regions, is also addressed. For experimental-demonstration purposes, an electronically-reconfigurable microstrip prototype of a two-stage-in-series-cascade dual-band NGD circuit is manufactured and measured.**

***Index Terms*— Absorptive filter, bandpass filter (BPF), band-stop filter (BSF), complementary diplexer, coupler, lossy filter, negative group delay (NGD), microstrip circuit, multi-functional circuit, planar circuit, reconfigurable circuit, reflectionless filter, RF analog signal processing, tunable circuit, wide-band filter.**

I. Introduction

THE DESIGN of RF/microwave circuits exhibiting a positive slope in the frequency-variation profile of their transfer-function phase, which are commonly referred to as "negative-group-delay (NGD) circuits", has attracted considerable research interest in the last few years as a particular class of RF-analog-signal-processing blocks [1], [2]. Due to the aforementioned property, they can be efficiently combined with more-conventional circuit networks having a negative transmission-phase slope to develop phase shifters [3], [4]. Other suitable applications of high-frequency NGD circuits include group-delay equalization in broad-band amplifiers [5], the reduction of signal-transmission delays in high-speed interconnects [6], bandwidth and efficiency improvement in linearized amplifiers [7]– [9], beam-squint prevention in phased-array antennas [10], [11], and the realization of non-Foster reactive elements—which can be used, for example, to enlarge tuning range in varactor diodes [12]– [15]. Despite several active-circuit-based approaches have been reported for NGD shaping especially when insertion loss is a concern as in [16]– [19], passive-NGD circuit solutions have become more popular due to their higher robustness against noise, intrinsic stability, and design simplicity.

It is well known that the realization of the NGD behavior in microwave passive—i.e., reciprocal—devices requires the incorporation of loss in their circuit structures [20]. Furthermore, such NGD characteristic is usually attained in narrow frequency ranges at the expense of perceptible in-band RF-signal-attenuation levels. Thus, most of the aforementioned applications of passive NGD circuits as, for example, those in [5], [7], and [11], have been carried out with the presence of active stages that help to compensate the extra insertion loss associated to these NGD stages. In addition, as a result of the inclusion of lossy elements in NGD networks, in-band RF-signal-power reflections may be created at the input access of the NGD circuit—since its input impedance becomes almost purely reactive—when the non-transmitted RF-signal energy is not fully dissipated into it. Such undesired in-band RF-signal-power echoes can deteriorate the behavior of preceding actives stages in RF front-end chains, e.g., by driving the amplifiers to operate in non-linear regime or by creating additional spurious terms in frequency-conversion stages [21]– [25]; even in lower-frequency scenarios they can lead to aliased harmonics coming from the switching transients inherent to analog-to-digital converters (ADCs) that the adjacent anti-aliasing filter is not capable of mitigating [26], [27]. To circumvent this problem, several techniques for low-reflection NGD circuit realization have been proposed. Among some others, as follows: (i) the addition of impedance transformers at the expense of reduced NGD depth and bandwidth [28], (ii) the utilization of lossy interconnecting lines between the ports of coupled-line couplers for low-attenuation NGD

Manuscript received November 10, 2020; revised January 8, 2021; accepted January 26, 2021. This work was supported in part by the Spanish Ministry of Economy, Industry, and Competitiveness (State Research Agency) under Project TEC2017-82398-R and in part by the National Science Foundation under Award 1731956. This article was recommended by Associate Editor M. Onabajo. *(Corresponding author: Roberto Gómez-García.)*

Roberto Gómez-García and José-María Muñoz-Ferreras are with the Department of Signal Theory and Communications, Polytechnic School, University of Alcalá, 28871 Alcalá de Henares, Spain (e-mail: roberto.gomez.garcia@ieee.org; jm.munoz@uah.es).

Dimitra Psychogiou was with the Department of Electrical, Computer and Energy Engineering, University of Colorado Boulder, Boulder, CO 80309 USA. She is now with the Department of Electrical and Electronic Engineering, University College Cork, Cork 021, T12 K8AF Ireland (e-mail: dpsychogiou@ucc.ie).

Color versions of one or more figures in this article are available at https://doi.org/10.1109/TCSI.2021.3055416.

Digital Object Identifier 10.1109/TCSI.2021.3055416

circuit designs that suffer from narrow-band behavior [29], (iii) the employment of lossy transversal-signal-interference circuit networks that achieve input/output power matching without external transformers for wide-band NGD responses but with low NGD depths as drawback [30], and (iv) the exploitation of absorptive NGD circuits that prevent RF-signal-power reflections by consuming all the non-transmitted signal energy into them [20], [31]. Nevertheless, all these approaches have been demonstrated in frequency-static NGD circuits without tuning capabilities. This supposes a lack for this type of devices when compared to other RF frequency-selective components for which the incorporation of spectral adaptivity has been already addressed, such as filters, diplexers, or filtering power dividers [32]– [35].

Owing to the growing necessity of flexible RF-analog-signal processors for widely-versatile high-frequency transceivers, the development of NGD circuits with reconfigurable spectral characteristics has also been addressed lately, although to a much lesser extent than their frequency-static counterparts. For example, in [36], a tunable NGD microstrip passive circuit based on a branch-line coupler that is loaded with variable resistors at two of its terminals was engineered. It features an NGD variation between -10 ns and -2 ns for its one-stage prototype and between -7 ns and -2.2 ns for its two-stage realization with enhanced bandwidth. However, the in-band insertion-loss level is simultaneously altered with the NGD tuning process due to the correlation between amplitude and phase responses. This effect is overcome in the active NGD circuit architecture reported in [37], which consists of a distributed-amplifier-based transversal-filter topology with stepped-impedance lines. It exhibits adaptable insertion-loss level for a nearly-constant NGD profile, therefore lacking of NGD control. As a further research step, NGD adjustment between -1.9 ns and -0.2 ns for a static insertion-loss profile was demonstrated in the NGD tuner conceived in [38]. It employs a transmission line that is loaded by a stub, two varactors, and a resistor. Nevertheless, its operational center frequency is fixed and no multi-stage in-series-cascade or higher-order designs are described to enable more-general NGD patterning. The NGD circuit network proposed in [39] exploits a resistorless quadruplet made up of tunable lossy/finite-quality-factor resonators to realize controllable NGD profile in terms of center frequency. However, its tuning capabilities are limited to the narrow frequency range of 2.02–2.2 GHz and only for a particular shape of NGD response. Finally, in [40], an NGD circuit concept based on two quadrature couplers that are loaded with varactors and inter-connected by means of amplifying stages is used for independent NGD and transmission-loss/gain control. However, no tuning capabilities in terms of center frequency and NGD profile—e.g., equi-ripple-NGD or flattened-NGD type—is verified. In addition, all these NGD circuit approaches detailed in [36]– [40] are focused on mono-band applications, so that their extension to multi-band designs has not been demonstrated. In relation with the latter, it should be noticed that even less efforts have been done on multi-band NGD circuit design. Indeed, only very few multi-band NGD devices are available in the technical literature, as the preliminary study in [41] where the synthesized NGD profile has a frequency-periodic pattern and no practical validation is shown. Hence, as of today, there is a full lack of flexible multi-band NGD circuits featuring low-RF-signal-power reflection and NGD reconfigurability for their operational bands in terms of center frequencies and NGD bandwidths/shapes.

As the extension of the single-band NGD circuit principle that was reported in [42], two distinct approaches of microwave NGD circuit stages with multi-band operation, one/two-port low-RF-signal-power-reflection characteristics, and spectral-adaptivity capabilities are presented in this paper. They are based on reconfigurable multi-band lossy-coupled-resonator topologies that are arranged in complementary-diplexer architectures. In this manner, the reflectionless property is attained for all the tuned states when the peer resonators in the main bandstop-filter-(BSF)-type and auxiliary bandpass-filter-(BPF)-type channels of the diplexer are synchronously controlled. These multi-band NGD stages can also be extended to higher-order and in-series-cascade designs, so that a large variety of NGD shapes can be patterned—e.g., equi-ripple-NGD, flattened-NGD, and maximum-NGD type. Furthermore, they can be co-integrated with other classes of RF passive circuits for the conception of new families of multi-functional microwave devices with embedded NGD bands along with their inherent RF-analog-signal-processing action.

The organization of the rest of the manuscript is as follows. In Section II, the theoretical operational foundations in terms of coupling-routing diagram of the engineered reflectionless multi-band NGD stages—coupling-resonating-node analytical framework that is general for any analog-circuit technology and frequency band [43]– [45]—are described. This includes input-reflectionless and two-port-quasi-reflectionless realizations, higher-order topologies, in-series cascade architectures, and their incorporation in broad-band BPFs and directional couplers for more-general NGD patterning with co-designed RF functionalities. Moreover, in the first-order case, guidelines for the synthesis of the input-reflectionless NGD stage in the bandpass domain are provided. For experimental-validation purposes, a varactor-tuned microstrip prototype of a two-stage-cascade dual-band NGD circuit is developed and tested in Section III. Finally, the summary and the most relevant concluding remarks of this work are set out in Section IV.

II. Theoretical Foundations

In this section, the theoretical operational principles of the two devised approaches of multi-band NGD circuits with low-reflection behavior are presented. First, the input-reflectionless architectures of their basic first-order stages are introduced, along with illustrative theoretical design examples. Subsequently, higher-order and in-series-cascaded multi-stage input-reflectionless schemes for broader-band and more-arbitrary NGD shaping with sharper transitions between positive and negative group-delay regions are described. The extrapolation of these multi-band NGD concepts to symmetrical/two-port quasi-reflectionless realizations is also addressed. Finally, examples of multi-functional devices, in which these multi-band NGD stages are embedded to produce NGD bands along with their intrinsic RF-analog-signal-processing action, are shown.

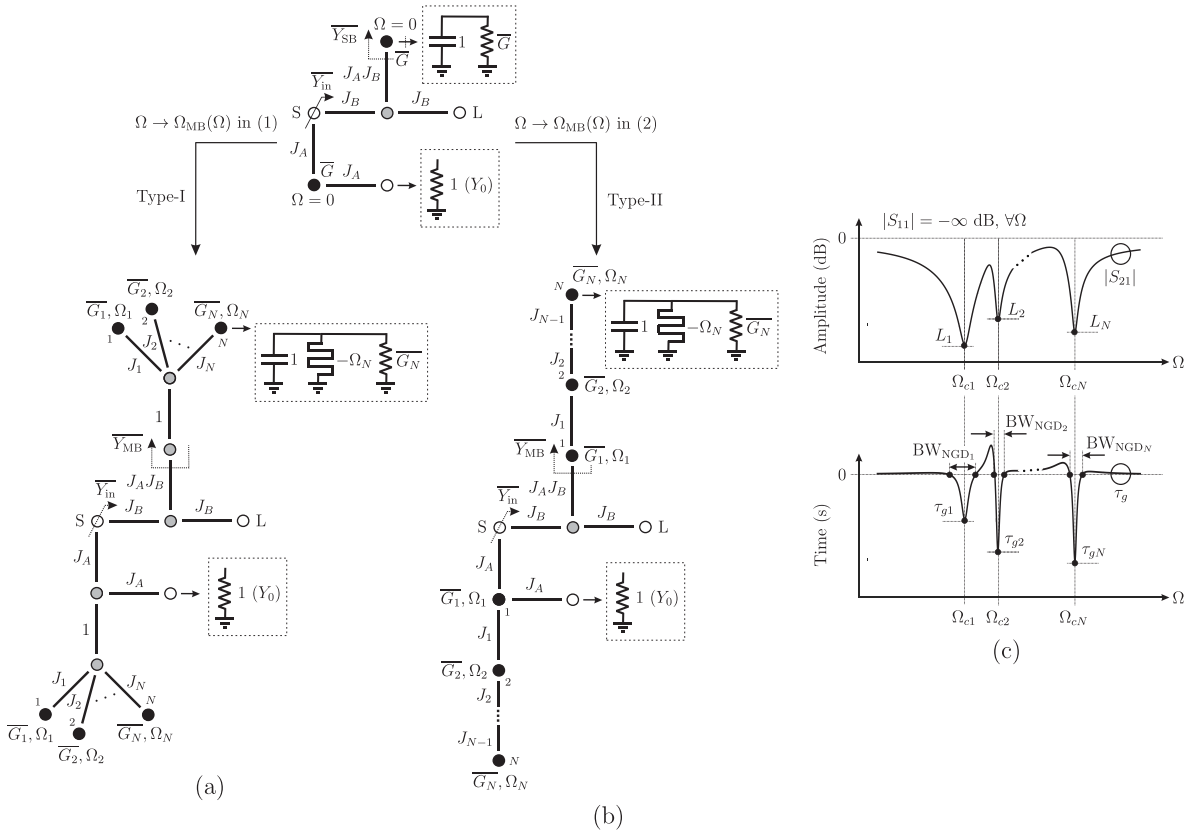

Fig. 1. Normalized coupling-routing diagram and conceptual power-transmission ($|S_{21}|$) and group-delay (τ_g) responses of the proposed input-reflectionless multi-band NGD stages for first-order N-band realizations. (a) Type-I multi-band NGD stage. (b) Type-II multi-band NGD stage. (c) Conceptual $|S_{21}|$ and τ_g.

A. Input-Reflectionless Multi-Band NGD Stages

The normalized coupling-routing diagrams of the two proposed types of input-reflectionless multi-band NGD stages—Type I and Type II—for an N-band first-order realization are depicted in Fig. 1(a) and (b), respectively. Their conceptual power transmission and group-delay responses are illustrated in Fig. 1(c). In these figures, the following notation is adopted:

- Black circles: lossy resonating nodes; grey circles: zero-susceptance non-resonating nodes (NRNs); white circles: unitary source (S), load (L), and loading resistor; continuous lines: couplings; $Y_0 = 1/Z_0$: reference admittance for normalization; $\overline{Y_{\text{in}}}$, $\overline{Y_{\text{SB}}}$, and $\overline{Y_{\text{MB}}}$: normalized input, single-band, and multi-band admittances; $J_A, J_B, J_1, J_2, \ldots, J_N$ variables: normalized admittance-inverter constants; $\overline{G_1}, \overline{G_2}, \ldots, \overline{G_N}$: normalized conductances; Ω (in rad/s): normalized frequency; $\Omega_i, \Omega_{ci}, \text{BW}_{\text{NGD}_i}, \tau_{gi}$, and L_i ($i = 1, 2, \ldots, N$): normalized resonant frequency of the ith resonator in the N-band resonant branch, normalized center frequency of the ith band, normalized NGD bandwidth of the ith band, NGD value at Ω_{ci}, and insertion-loss level at Ω_{ci}.

As can be seen in Fig. 1, they are based on a first-order lossy-complementary-diplexer architecture, in which the NGD bands are located within the stopband regions of the lossy first-order multi-band-BSF channel—i.e., main channel. The lossy first-order multi-band-BPF channel—i.e., auxiliary channel—is terminated by a resistor that absorbs the non-transmitted RF-input-signal energy by the main channel within its stopbands. In this manner, perfect input-reflectionless capabilities—i.e., zero RF-input-power reflection at any frequency since the condition $\overline{Y_{\text{in}}}(\Omega) = 1$, $\forall\Omega$ is satisfied—are obtained in the overall stages. It should be remarked upon that, as illustrated in Fig. 1, the two input-reflectionless multi-band NGD stages in Fig. 1(a) and (b) can be derived from its single-band precursor proposed in [42] after applying appropriate complex-number variable transformations $\Omega \rightarrow \Omega_{\text{MB}}(\Omega)$ as detailed in (1) and (2). They equivalently result in single-to-multi-band normalized-admittance transformations $\overline{Y_{\text{SB}}}(\Omega) \rightarrow \overline{Y_{\text{MB}}}(\Omega)$ in the normalized coupling-routing diagrams in Fig. 1(a) and (b) for the multi-band NGD patterning with regard to the single-band one.

- Type I:

$$\Omega \rightarrow \Omega_{\text{MB}}(\Omega) = j\left[\overline{G} - \left(\sum_{i=1}^{N} \frac{J_i^2}{\overline{G_i} + j(\Omega - \Omega_i)}\right)^{-1}\right] \tag{1}$$

- Type II:

$$\Omega \rightarrow \Omega_{\text{MB}}(\Omega) = \Omega - \Omega_1 + j\left[\overline{G} - \overline{G_1} - \cfrac{J_1^2}{\overline{G_2} + j(\Omega - \Omega_2) + \cfrac{J_2^2}{\cdots + \cfrac{J_{N-1}^2}{\overline{G_N} + j(\Omega - \Omega_N)}}}\right]. \tag{2}$$

It should be highlighted that the fundamental principle for input-reflectionless multi-stopband generation in the Type-I and Type-II stages is different. Specifically, when lossless resonating nodes are assumed—i.e., $\overline{G_1} = \overline{G_2} = \ldots = \overline{G_N} = 0$ which results in zero-bandwidth NGD bands—, the normalized center frequencies of the stopbands in the Type-I stage are equal to the resonant frequencies of the resonating nodes—i.e., $\Omega_{ci} = \Omega_i$, $i = 1, 2, \ldots, N$. Nevertheless, in the Type-II stage and under the same conditions, they are produced by means of a split-type phenomenon so that they are as follows for the dual-band case—i.e., $N = 2$—as an illustrative example:

$$\Omega_{c1}, \Omega_{c2} = \frac{\Omega_1 + \Omega_2 \pm \sqrt{(\Omega_1 - \Omega_2)^2 + 4J_1^2}}{2}. \tag{3}$$

When lossy resonating nodes are considered—i.e., finite-bandwidth NGD bands—, the normalized center frequencies are slightly modified from the previous ones depending on the values of the normalized conductances of the resonating nodes.

The formulas of the power transmission parameter, $S_{21}(\Omega)$, and group-delay function, $\tau_g(\Omega)$, for the two types of input-reflectionless multi-band NGD stages in Fig. 1(a) and (b) are

$$S_{21}(\Omega) = -\frac{\overline{G} + j\Omega_{\text{MB}}(\Omega)}{\overline{G} + J_A^2 + j\Omega_{\text{MB}}(\Omega)} \tag{4}$$

$$\begin{aligned}\tau_g(\Omega) &= -\frac{\measuredangle\{S_{21}(\Omega)\}}{d\Omega} \\ &= \left[-\frac{\overline{G}}{\overline{G}^2 + \Omega_{\text{MB}}^2(\Omega)} + \frac{\overline{G} + J_A^2}{\left(\overline{G} + J_A^2\right)^2 + \Omega_{\text{MB}}^2(\Omega)}\right] \\ &\quad \times \left(\frac{d\Omega_{\text{MB}}(\Omega)}{d\Omega}\right)\end{aligned} \tag{5}$$

where $\Omega_{\text{MB}}(\Omega)$ is given by (1) and (2) for the Type-I and Type-II input-reflectionless multi-band NGD stages, respectively.

For the input-reflectionless single-band NGD stage at the top of Fig. 1—i.e., $N = 1$—, from (3) and (4) after applying the inverse transformation $\Omega_{\text{MB}}(\Omega) \rightarrow \Omega$, the theoretical expressions below for the NGD at $\Omega = 0$, τ_{g0}, NGD bandwidth, BW_{NGD}, and power-attenuation level at $\Omega = 0$, L_0, can be obtained as follows:

$$\tau_{g0} \equiv \tau_g(\Omega = 0) = -\frac{J_A^2}{\overline{G}\left(\overline{G} + J_A^2\right)} \tag{6}$$

$$\text{BW}_{\text{NGD}} = 2\sqrt{\overline{G}\left(\overline{G} + J_A^2\right)} = \frac{2|J_A|}{\sqrt{-\tau_{g0}}} \tag{7}$$

$$L_0\ (\text{dB}) \equiv -20\log_{10}|S_{21}(\Omega = 0)| = -20\log_{10}\left(\frac{\overline{G}}{\overline{G} + J_A^2}\right). \tag{8}$$

From (6)–(8), it can be deduced that a lower—i.e., more negative—value for τ_{g0} implies a smaller BW_{NGD} value for a fixed insertion-loss level L_0 at $\Omega = 0$. This reveals the design trade-off existing between these two NGD characteristics, as explicitly expressed by the following formulas that are derived from (6)–(8) (note that L_0 below is given in natural units):

$$\tau_{g0} = -\frac{J_A^2 L_0}{\overline{G}^2} = -\frac{4J_A^2}{\text{BW}_{\text{NGD}}^2} \qquad L_0 = \frac{4\overline{G}^2}{\text{BW}_{\text{NGD}}^2}. \tag{9}$$

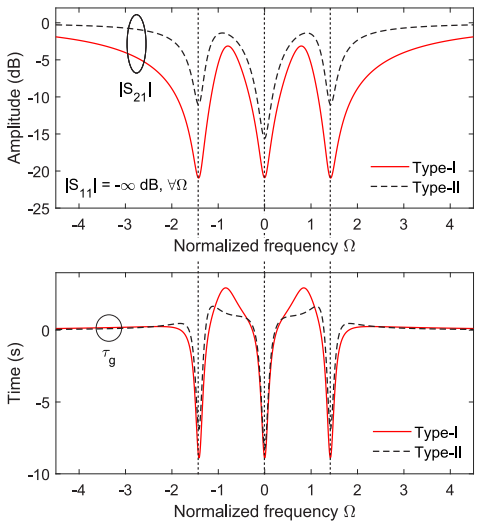

Fig. 2. Theoretical power transmission ($|S_{21}|$) and group-delay (τ_g) responses of the Type-I and Type-II input-reflectionless multi-band NGD stages in Fig. 1(a) and (b) for triple-band examples (Type-I: $\Omega_1 = -\Omega_3 = -\sqrt{2}$, $\Omega_2 = 0$, $\overline{G_1} = \overline{G_2} = \overline{G_3} = 0.1$, and $J_A = J_B = J_1 = J_2 = J_3 = 1$; Type-II: $\Omega_1 = \Omega_2 = \Omega_3 = 0$, $\overline{G_1} = \overline{G_2} = \overline{G_3} = 0.1$, and $J_A = J_B = J_1 = J_2 = 1$).

For the two input-reflectionless multi-band NGD stages in Fig. 1(a) and (b),—i.e., $N \geq 2$—, the derivation of analytical formulas for the previous parameters associated to each of the N NGD bands is more tedious. Nevertheless, conclusions from illustrative examples of represented theoretical power transmission and group-delay responses can be obtained, as follows:

- Three-band responses for the Type-I and Type-II input-reflectionless multi-band NGD stages in Fig. 1(a) and (b) are plotted in Fig. 2 for the case $\overline{G_1} = \overline{G_2} = \overline{G_3} \equiv \overline{G}$. As can be seen, for the Type-II stage, it results in different NGD depths at the center frequencies of the lower and upper bands with regard to the middle one due to inter-band interaction. Nevertheless, this can be counteracted by using different values for the normalized conductances of the resonating nodes in the multi-band NGD stage—i.e., distinct effective quality factors in their realization.
- For the Type-I input-reflectionless multi-band NGD stage as an example, different responses are depicted in Fig. 3. As observed, the previously-referred trade-off between the NGD bandwidth and depth at the center frequency for each band is also confirmed here, as an expected result considering that both networks in Fig. 1(a) are related one to the other through the variable transformation in (1).
- For the Type-I input-reflectionless multi-band NGD stage as an example, a triple-band response with strongly-asymmetrical NGD bandwidths and depths at the center frequencies for the three bands is provided in Fig. 4. Furthermore, a single-band equi-ripple-type NGD profile realized by closely positioning the three NGD bands is also drawn in Fig. 4, as verification of the NGD-patterning flexibility of the conceived multi-band NGD approach.

In relation to the results in Figs. 3 and 4, it should be emphasized that similar conclusions can be extracted

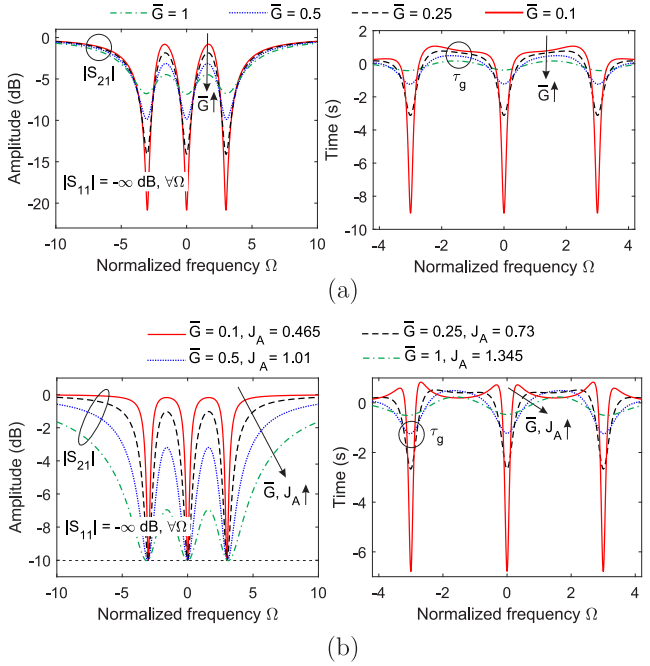

Fig. 3. Theoretical power transmission ($|S_{21}|$) and group-delay (τ_g) responses of the Type-I input-reflectionless multi-band NGD stage in Fig. 1(a) for triple-band examples: influence of the design variables. (a) Influence of $\overline{G_1} = \overline{G_2} = \overline{G_3} \equiv \overline{G}$ ($\Omega_1 = -\Omega_3 = -3$, $\Omega_2 = 0$, and $J_A = J_B = J_1 = J_2 = J_3 = 1$ in all cases). (b) Influence of $\overline{G_1} = \overline{G_2} = \overline{G_3} \equiv \overline{G}$ and J_A for fixed NGD depths of 10 dB ($\Omega_1 = -\Omega_3 = -3$, $\Omega_2 = 0$, and $J_B = J_1 = J_2 = J_3 = 1$ in all cases).

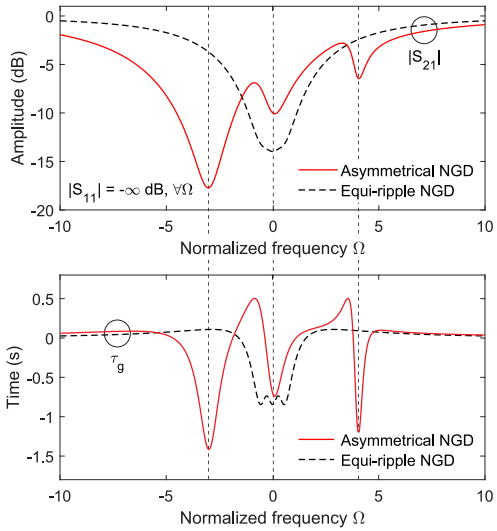

Fig. 4. Theoretical power transmission ($|S_{21}|$) and group-delay (τ_g) responses of the Type-I input-reflectionless multi-band NGD stage in Fig. 1(a) for asymmetrical-NGD triple-band and equi-ripple-NGD single-band examples (triple-band: $\Omega_1 = -3$, $\Omega_2 = 0$, $\Omega_3 = 4$, $\overline{G_1} = \overline{G_2} = 0.6$, $\overline{G_3} = 0.3$, $J_A = J_B = J_2 = 1$, $J_1 = 2$, and $J_3 = 0.5$; equi-ripple: $\Omega_1 = -\Omega_3 = -0.5$, $\Omega_2 = 0$, $\overline{G_1} = \overline{G_3} = 0.53$, $\overline{G_2} = 0.5$, and $J_A = J_B = J_1 = J_2 = J_3 = 1$).

for the Type-II input-reflectionless multi-band NGD stage. Hence, the convenience of using one or another solution of multi-band NGD topology is mostly determined by the suitability of implementing one or another coupling-routing diagram in the selected technology. Moreover, spectral adaptivity can be added to these multi-band NGD circuit networks by making their resonating nodes frequency tunable with the inclusion of variable-reactance elements. In this manner, a large variety of multi-band NGD profiles can be configured in the same circuit.

B. Synthesis in the Bandpass Domain

In Section II.A, the theoretical foundations of the proposed input-reflectionless multi-band NGD stages—Type I and Type II—for first-order N-band realizations in terms of coupling-routing diagrams in the normalized lowpass frequency domain have been described. However, their synthesis in the bandpass domain for a Y_0 admittance level can be performed by using a lowpass-to-bandpass frequency transformation $\Omega \rightarrow \Omega_{\rm BP}(f)$ over the single-band normalized network at the top of Fig. 1 and appropriate Y_0-admittance scaling of its circuit elements.

For example, for the Type-I multi-band NGD stage, the corresponding lowpass-to-bandpass frequency transformation $\Omega \rightarrow \Omega_{\rm BP}(f)$ for an N-NGD-band realization is as follows:

$$\Omega \rightarrow \Omega_{\rm BP}(f) = j\left[\overline{G} - \left(\sum_{i=1}^{N} \frac{J_i^2}{\overline{G_i} + \frac{j}{\alpha_i}\left(\frac{f}{f_{ci}} - \frac{f_{ci}}{f}\right)}\right)^{-1}\right] \tag{10}$$

where f_{ci} and α_i ($i = 1, 2, \ldots, N$) are the center frequency and bandwidth-scaling factor of the ith NGD band in the bandpass domain, respectively. From (10), the following cases are distinguished depending on the selection of the N value:

- For $N = 1$ and assuming that $\overline{G_1} = \overline{G}$ and $J_1 = 1$ without any loss of generality, (10) turns out to be the well-known lowpass-to-bandpass frequency transformation:

$$\Omega_{\rm BP}(f) = \frac{1}{\alpha_1}\left(\frac{f}{f_{c1}} - \frac{f_{c1}}{f}\right). \tag{11}$$

  By using (11), a correspondence between the NGD design parameters in the bandpass and normalized lowpass frequency domains can be established. Thus, the following design procedure can be adopted to synthesize the NGD network in the bandpass domain for a Y_0 admittance level from the desired NGD value at the center frequency f_{c1} and NGD bandwidth, $\tau_{g1}^{\rm BP}$ and $\mathrm{BW}_{\mathrm{NGD}_1}^{\rm BP}$, respectively:

  1) From f_{c1}, $\tau_{g1}^{\rm BP}$, and $\mathrm{BW}_{\mathrm{NGD}_1}^{\rm BP}$ obtain the values for the parameters τ_{g0} and $\mathrm{BW}_{\rm NGD}$ of the associated normalized coupling-routing diagram in Fig. 1 as follows—α_1 is a degree of freedom that does not have any influence on the synthesized response:

$$\tau_{g0} = (\pi\,\alpha_1\ f_{c1})\,\tau_{g1}^{\rm BP}$$
$$\mathrm{BW}_{\rm NGD} = \left(\frac{2}{\alpha_1\ f_{c1}}\right)\mathrm{BW}_{\mathrm{NGD}_1}^{\rm BP}. \tag{12}$$

  2) Determine the values of the normalized circuit elements J_A and $\overline{G}$ as indicated below:

$$J_A = \frac{\mathrm{BW}_{\rm NGD}\sqrt{-\tau_{g0}}}{2}$$
$$\overline{G} = -\left(\frac{J_A^2\tau_{g0} + \sqrt{J_A^4\tau_{g0}^2 - 4J_A^2\tau_{g0}}}{2\tau_{g0}}\right). \tag{13}$$

  3) Calculate the values of the denormalized admittance inverters K_A and K_B and lossy-resonator elements

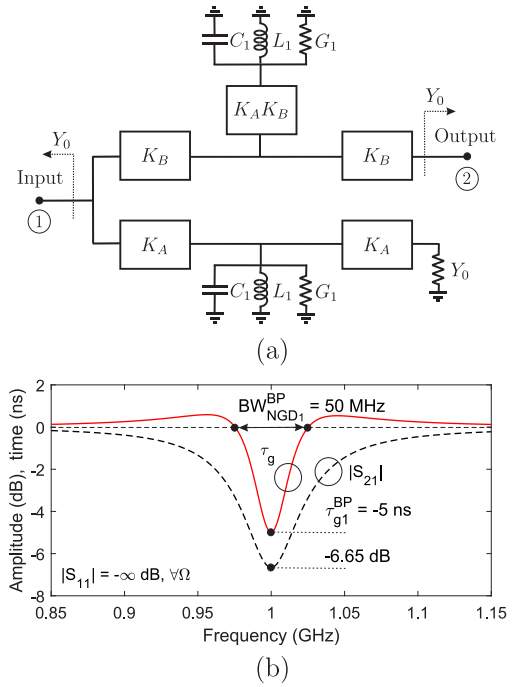

Fig. 5. Input-reflectionless single-band—i.e., $N = 1$—NGD stage in the bandpass frequency domain. (a) Circuit scheme. (b) Power transmission ($|S_{21}|$) and group-delay (τ_g) responses of a theoretical design example for $Y_0 = 0.02$ S—i.e., $Z_0 = 50\ \Omega$—, $f_{c1} = 1$ GHz, $\tau^{BP}_{g1} = -5$ ns, and $BW^{BP}_{NGD_1} = 50$ MHz ($K_A = 0.0117$ S, $G_1 = 0.0136$ S, $L_1 = 0.398$ nH, and $C_1 = 63.66$ pF; $\alpha_1 = 0.05$ in this example and K_B is set as desired).

G_1, L_1, and C_1—see Fig. 5(a)—as follows—J_B is a degree of freedom that does not have any influence in the synthesized response:

$$K_A = J_A Y_0 \qquad K_B = J_B Y_0 \qquad G_1 = \overline{G} Y_0$$
$$L_1 = \frac{\alpha_1}{2\pi f_{c1} Y_0} \qquad C_1 = \frac{Y_0}{2\pi f_{c1} \alpha_1}. \tag{14}$$

The single-band NGD circuit network in the bandpass domain designed through the previous procedure is shown in Fig. 5(a). For illustration purposes, Fig. 5(b) depicts the NGD profile and power transmission response for a synthesis example with $f_{c1} = 1$ GHz, $\tau^{BP}_{g1} = -5$ ns, and $BW^{BP}_{NGD_1} = 50$ MHz, where the values of the circuit elements derived from (14) are listed in its caption. Note that the insertion-loss level at the NGD-band center frequency is the one of its lowpass counterpart as in (8).

- For $N \geq 2$, the derivation of exact synthesis formulas as for $N = 1$ may be unfeasible, due to the mathematical difficulty involved in establishing a closed-formula mapping between the NGD parameters in the bandpass and normalized lowpass domains. Nevertheless, when the interaction between the different bands is negligible—i.e., widely-separated and spectrally-narrow NGD bands—, the design procedure expounded for the case $N = 1$ can be adopted to synthesize each NGD band separately by assuming that $J_1 = J_2 = \ldots = J_N = 1$ without any loss of generality—as when the inter-NGD-band interaction is significant, the use of inspection-based numerical techniques for the exact synthesis process is needed. Note that, in this case, as the normalized admittance inverter J_A is common to shape all the NGD bands, the same value for it must be derived with (13) when synthesizing each band. Once α_1 is chosen as a degree of freedom so that $J_{A1} \equiv J_A$ is obtained in the synthesis of the first NGD band, this is done by setting the bandwidth-scaling factors α_k for the remaining $N - 1$ NGD bands as

$$\alpha_k = \frac{\pi \left(BW^{BP}_{NGD_k}\right)^2 (-\tau^{BP}_{gk})}{J_A^2 f_{ck}}, \quad k = 2, 3, \ldots, N. \tag{15}$$

A synthesized example of dual-band NGD circuit network for $f_{c1} = 0.7$ GHz, $f_{c2} = 1.3$ GHz, $\tau^{BP}_{g1} = -8$ ns, $\tau^{BP}_{g2} = -3$ ns, $BW^{BP}_{NGD_1} = 30$ MHz, and $BW^{BP}_{NGD_2} = 70$ MHz is provided in Fig. 6, for which the computed values for the circuit elements are indicated in its caption.

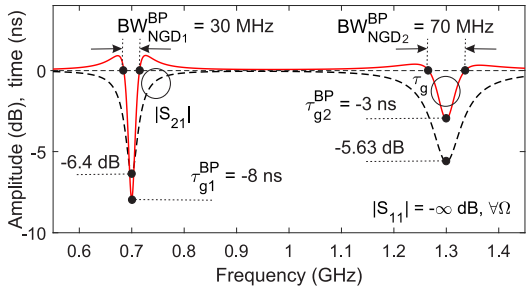

Fig. 6. Power transmission ($|S_{21}|$) and group-delay (τ_g) responses of a theoretical design example of input-reflectionless dual-band—i.e., $N = 2$—NGD stage in the bandpass frequency domain for $Y_0 = 0.02$ S—i.e., $Z_0 = 50\ \Omega$—, $f_{c1} = 0.7$ GHz, $f_{c2} = 1.3$ GHz, $\tau^{BP}_{g1} = -8$ ns, $\tau^{BP}_{g2} = -3$ ns, $BW^{BP}_{NGD_1} = 30$ MHz, and $BW^{BP}_{NGD_2} = 70$ MHz ($K_A = 0.0208$ S, $K_1 = K_2 = 0.02$ S, $G_1 = 0.0198$ S, $L_1 = 0.341$ nH, $C_1 = 151.58$ pF, $G_2 = 0.0236$ S, $L_2 = 0.202$ nH, and $C_2 = 74.2$ pF; $\alpha_1 = 0.03$ in this example, $\alpha_2 = 0.033$ as derived from (15), and K_B is set as desired).

C. Higher-Order and Multi-Stage Multi-Band NGD Designs

Input-reflectionless multi-band NGD circuits for higher-order and in-series-cascaded multi-stage schemes can be designed. They allow for wider-band and more-general multi-band NGD profiles with sharper transitions between positive and negative group-delay regions to be patterned for the Type-I and Type-II multi-band NGD stages in Fig. 1(a) and (b).

For illustration purposes, Fig. 7 shows the normalized coupling-routing diagram corresponding to the Kth-order generalization of the Type-I N-band NGD stage in Fig. 1(a). By following an analogous procedure to the one described in [46], design formulas for the normalized admittance inverters enabling zero-RF-input-power reflection to be attained at any frequency can be derived—see Table I in Section II.A in [46] for the Kth-order single-band counterpart in Fig. 1(b) therein after assuming lossy resonators with $\overline{G}$ normalized conductance, from which the multi-band NGD circuit network in Fig. 7 can be obtained by applying the variable transformation in (1).

Associated to Fig. 7, dual-band examples—i.e., $N = 2$—of theoretical power transmission and group-delay responses for first-to-fourth-order realizations—i.e., $K = 1, 2, 3$, and 4—are depicted in Fig. 8. These examples were obtained for identical NGD bandwidths in their bands for comparison purposes. As can be seen, as the order increases, higher NGD depths at the center frequencies—i.e., more negative values—are

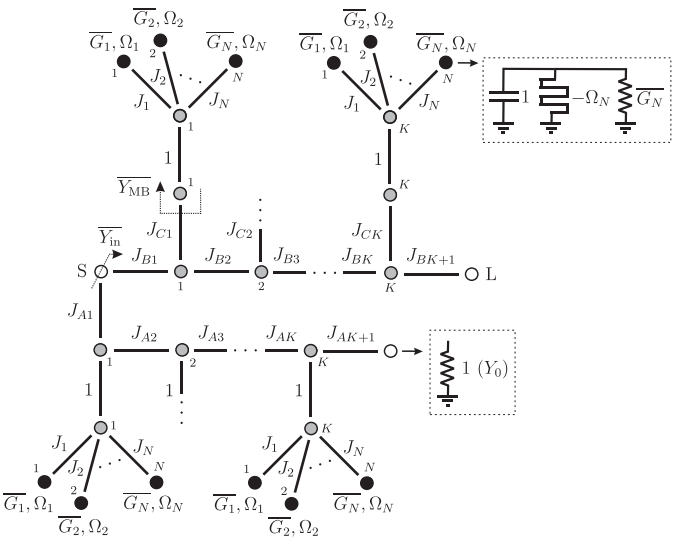

Fig. 7. Normalized coupling-routing diagram of the multi-band NGD circuit associated to the Type-I multi-band NGD stage in Fig. 1(a) for a Kth-order N-band realization.

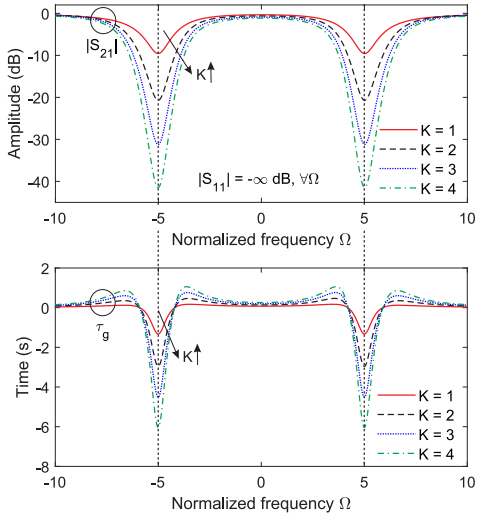

Fig. 8. Theoretical power transmission ($|S_{21}|$) and group-delay (τ_g) responses of the Type-I first-to-fourth-order—i.e., $K = 1, 2, 3, 4$—N-band NGD circuit in Fig. 7 for dual-band examples with equal NGD bandwidths ($\Omega_1 = -\Omega_2 = -5$ and $\overline{G_1} = \overline{G_2} = 0.5$ in all examples): $K = 1$: $J_A = J_B = 1$ and $J_1 = J_2 = 1$; $K = 2$: $J_{A1} = J_{B1} = J_{B2} = J_{B3} = J_{C2} = 1$, $J_{A2} = J_{A3} = J_{C1} = 1.4141$, and $J_1 = J_2 = 1$; $K = 3$: $J_{A1} = 1.1547$, $J_{A2} = 1.4142$, $J_{A3} = 2.4495$, $J_{A4} = 2$, $J_{B1} = J_{B2} = J_{B3} = J_{B4} = J_{C3} = 1$, $J_{C1} = 1.7321$, $J_{C2} = 1.633$, and $J_1 = J_2 = 0.8$; $K = 4$: $J_{A1} = 1.3066$, $J_{A2} = J_{C3} = 1.6818$, $J_{A3} = J_{C1} = 2$, $J_{A4} = 4.0602$, $J_{A5} = 2.6131$, $J_{B1} = J_{B2} = J_{B3} = J_{B4} = J_{B5} = J_{C4} = 1$, $J_{C2} = 2.0301$, and $J_1 = J_2 = 0.7$.

achieved, which results in sharper transitions between positive and negative group-delay regions. Note that this is done at the expense of higher attenuation levels at the center frequencies of the stopbands, as an expected result owing to the employment of a higher number of lossy resonating nodes in the dual-band-BSF-type channel of the overall circuit.

In-series-cascaded multi-stage designs aimed at the shaping of more-arbitrary and wider-band multi-band NGD profiles can also be carried out. This can be performed either by cascading several basic multi-band NGD stages and/or higher-order stages without inter-section matching elements, due to

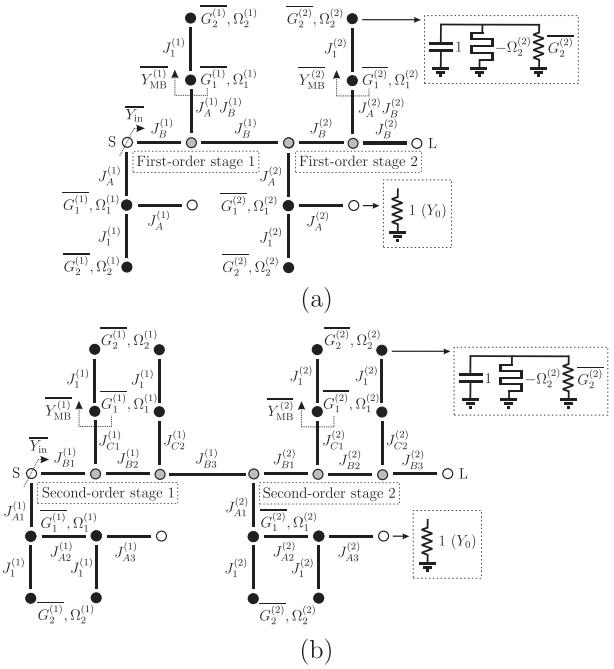

Fig. 9. Normalized coupling-routing diagram of the dual-band NGD circuits based on the in-series cascade of two Type-II first-order and second-order dual-band NGD stages. (a) First-order cascade. (b) Second-order cascade.

the perfect input-reflectionless nature of all these constituent stages which are preserved in the overall circuit. As an example, Fig. 9(a) and (b) represent the normalized coupling-routing diagrams of the in-series cascade of two first-order and two second-order Type-II dual-band NGD stages, respectively, whose peer resonating nodes are tuned at different normalized frequencies in each stage. In this case, the overall power transmission and group-delay responses are the product and the sum, respectively, of those associated to each building stage due to their RF-input-reflectionless behavior, which assure perfect Z_0-impedance-matching at all frequencies for all stages.

Figure 10 depicts the theoretical power transmission and group-delay responses, along with those corresponding to their constituent stages, of dual-band NGD examples for the circuit architectures in Fig. 9(a) and (b). In these examples, the two constituent stages are closely positioned to shape an overall wider-band and flattened dual-band NGD profile and have been designed to exhibit the same NGD bandwidths in both bands. As can be seen in Fig. 10, in coherence with the results in Fig. 8, more-negative NGD values at the center frequencies of the NGD dual bands are attained as the order increases. Note that this design methodology can be equally applied to the spectral shaping of other classes of broader-band group-delay patterns, such as equi-ripple-type ones like in Fig. 4.

D. Symmetrical Reflectionless Multi-Band NGD Networks

The conceived approaches of Type-I and Type-II multi-band NGD stages, as well as their higher-order and in-series-cascade multi-stage realizations, can be extended to symmetrical architectures with reflectionless behavior at both the input and output ports. To this aim, an absorptive lossy multi-band-BPF-type branch must be loaded at both the input and output nodes to dissipate out-of-band RF-power-reflections at both accesses.

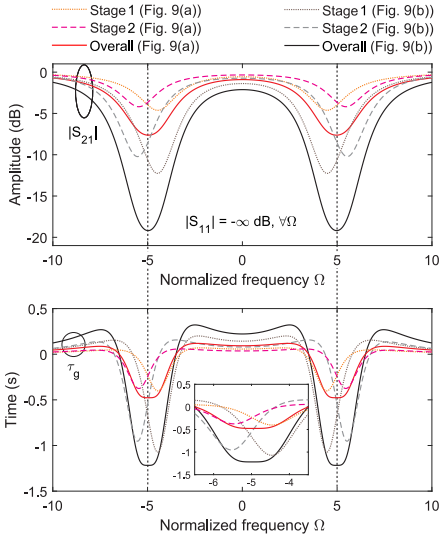

Fig. 10. Examples of theoretical power transmission ($|S_{21}|$) and group-delay (τ_g) responses of the Type-II in-series-cascade dual-band NGD circuits in Fig. 9(a) and (b) (Example of Fig. 9(a): $\Omega_1^{(1)} = \Omega_2^{(1)} = \Omega_1^{(2)} = \Omega_2^{(2)} = 0$, $\overline{G_1^{(1)}} = \overline{G_2^{(1)}} = \overline{G_1^{(2)}} = \overline{G_2^{(2)}} = 1$, $J_A^{(1)} = 1.1761$, $J_B^{(1)} = J_B^{(2)} = 1$, $J_1^{(1)} = 4.4382$, $J_A^{(2)} = 1.1073$, and $J_1^{(2)} = 5.4472$; Example of Fig. 9(b): $\Omega_1^{(1)} = \Omega_2^{(1)} = \Omega_1^{(2)} = \Omega_2^{(2)} = 0$, $\overline{G_1^{(1)}} = \overline{G_2^{(1)}} = \overline{G_1^{(2)}} = \overline{G_2^{(2)}} = 1$, $J_{A1}^{(1)} = 0.9514$, $J_{A2}^{(1)} = 1$, $J_{A3}^{(1)} = 1.0511$, $J_{B1}^{(1)} = 1.2875$, $J_{B2}^{(1)} = 2.3443$, $J_{B3}^{(1)} = 1.8208$, $J_{C1}^{(1)} = 1.7323$, $J_{C2}^{(1)} = 1.3533$, $J_1^{(1)} = 4.4454$, $J_{A1}^{(2)} = 1.2364$, $J_{A2}^{(2)} = 1$, $J_{A3}^{(2)} = 0.8088$, $J_{B1}^{(2)} = 1.1532$, $J_{B2}^{(2)} = 1.8807$, $J_{B3}^{(2)} = 1.6309$, $J_{C1}^{(2)} = 2.0164$, $J_{C2}^{(2)} = 0.9327$, and $J_1^{(2)} = 5.5105$).

For illustration purposes, Fig. 11(a) and (b) depict the normalized coupling-routing diagram and the theoretical power transmission and group-delay response for a two-port-reflectionless example of second-order dual-band NGD realization for the Type-I network. Note that the same NGD bandwidths and values for the normalized conductances as in the input-reflectionless second-order dual-band example in Fig. 8 have been selected to compare with. As shown, as the main conclusion to be extracted and whereas the insertion-loss level at the center frequencies of the NGD bands and the NGD depths are higher in the two-port-symmetrical case due to the inclusion of more lossy resonators, a quasi-reflectionless behavior instead of a perfect-reflectionless one is attained in the symmetrical example. Nevertheless, power-matching levels above 20 dB are obtained at all frequencies in the two-port-reflectionless case, as validation of this design methodology for two-port-low-reflection multi-band NGD circuits.

E. Reflectionless Passive Devices With Embedded NGD Bands

Low-reflection multi-functional microwave passive devices, in which several NGD bands can be produced along with their inherent RF-analog-processing action within their operational bandwidth in the same circuit volume, can be designed. They feature more-compact size, lower insertion loss, and enhanced performance when compared to cascades of mono-functional blocks due to the avoidance of inter-connection stages between them and the need for Z_0 impedance matching at each block. In particular, as illustrative examples, wide-band BPFs and directional couplers with embedded NGD bands are considered.

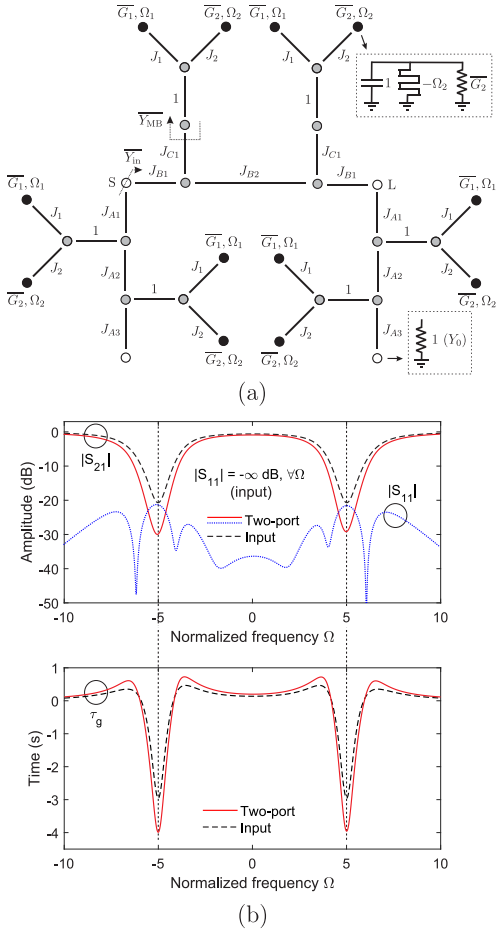

Fig. 11. Normalized coupling-routing diagram and example theoretical power transmission ($|S_{21}|$), input-reflection ($|S_{11}|$), and group-delay (τ_g) responses (compared with its input-reflectionless counterpart—i.e., $K = 2$—in Fig. 8) of Type-I symmetrical-reflectionless second-order dual-band NGD circuit. (a) Normalized coupling-routing diagram. (b) $|S_{21}|$, $|S_{11}|$, and τ_g (two-port-quasi-reflectionless: $\Omega_1 = -\Omega_2 = -5$, $\overline{G_1} = \overline{G_2} = 0.5$, $J_{A1} = 0.9432$, $J_{A2} = 1.3162$, $J_{A3} = 1.7719$, $J_{B1} = 1.0133$, $J_{B2} = 1.0103$, $J_{C1} = 1.3196$, $J_1 = 1.0077$, and $J_2 = 0.9848$).

1) Wide-Band BPFs With Embedded NGD Bands: Broad-band BPFs with inserted NGD bands in their passband range can be designed by properly modifying the normal-ized coupling-routing diagrams of the Type-I and Type-II multi-band NGD networks in any of the previously-discussed realizations. For illustration purposes, Fig. 12(a) shows the normalized coupling-routing diagram of an input-reflectionless third-order BPF with two inserted third-order NGD bands based on the Type-I solution. As can be seen, with regard to the scheme in Fig. 7 for $K = 3$ and $N = 2$, the NRNs interacting with the two resonating nodes—shaping of NGD bands—in each stage are replaced by lossless resonating nodes that conform the wide passband centered at the normalized frequency Ω_0. Examples of theoretical power transmission and group-delay responses for the circuit architecture in Fig. 12(a) are depicted in Fig. 12(b) for spectrally-symmetrical and asym-metrical embedded NGD bands, which reveals the suitability of the suggested design approach. Note that higher in-band insertion-loss levels are produced in the passband range when more-lossy resonating nodes are considered, as their expected in-band influence outside the NGD regions.

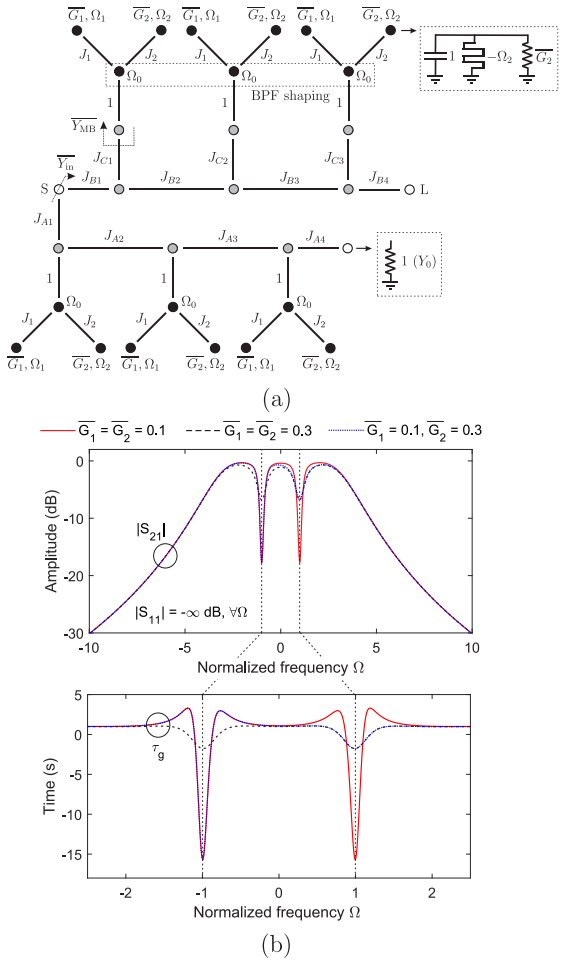

Fig. 12. Normalized coupling-routing diagram and example theoretical power transmission ($|S_{21}|$) and group-delay (τ_g) responses of Type-I input-reflectionless third-order BPF with two embedded third-order NGD bands. (a) Normalized coupling-routing diagram. (b) $|S_{21}|$ and τ_g ($\Omega_0 = 0$, $\Omega_1 = -\Omega_2 = -1$, $J_{A1} = 0.4619$, $J_{A2} = 0.2263$, $J_{A3} = 0.3919$, $J_{A4} = 0.8$, $J_{B1} = J_{B4} = 1$, $J_{B2} = J_{B3} = J_{C3} = 0.4$, $J_{C1} = 0.6928$, $J_{C2} = 0.2613$, and $J_1 = J_2 = 0.6$ in all cases).

2) Directional Couplers With Embedded NGD Bands: The devised lossy-complementary-diplexer-based multi-band NGD approach can be also co-integrated with other RF passive devices, such as directional couplers. Based on the Type-II solution, Fig. 13(a) depicts the normalized coupling-routing diagram of a modified input-reflectionless out-of-phase directional coupler by adding second-order lossy-dual-band-BSF-type branches in the direct and coupled paths. Note that a single lossy-dual-band-BPF-type arm is loaded at the input port to attain the zero-input-reflection property. In this manner, this triple-functionality component allows to perform the out-of-phase coupler functionality, while simultaneously featuring two second-order input-reflectionless NGD bands within the input-to-direct/coupled-port transfer functions. Figure 13(b) depicts the power transmission and group-delay responses for several examples with 3-dB coupling factor. As proven, a perfect input-reflectionless behavior and isolation between the two out-of-phase output terminals at all frequencies is attained in all cases. Moreover, similar trends as those shown by the previous examples regarding the NGD-band creation are observed.

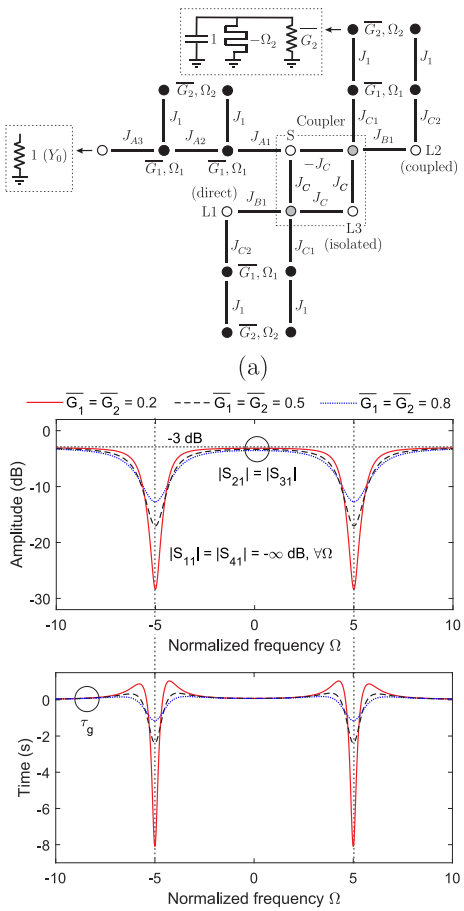

Fig. 13. Normalized coupling-routing diagram and example theoretical power transmission ($|S_{21}|$ and $|S_{31}|$) and group-delay (τ_g) responses of Type-II fully-input-reflectionless out-of-phase 3-dB coupler with perfect isolation and two embedded second-order NGD bands. (a) Normalized coupling-routing diagram. (b) $|S_{21}|$, $|S_{31}|$, and τ_g ($\Omega_1 = \Omega_2 = 0$, $J_C = 1/\sqrt{2}$, and $J_{A1} = J_{C2} = 1$, $J_{A2} = J_{A3} = J_{B1} = \sqrt{2}$, $J_{C1} = 2$, and $J_1 = 5$ in all cases).

III. Experimental Results

To demonstrate the practical feasibility of the engineered low-reflection multi-band NGD circuit networks, a frequency-adaptive microstrip prototype has been developed and tested. It corresponds to a 50-Ω-referred electronically-tunable realization of an in-series cascade of two Type-I dual-band NGD stages. It was initially designed to feature reconfigurable NGD bands within the frequency range 1.5–2 GHz, which are shaped from the congregation of the narrower NGD dual bands of its two constituent spectrally-adjacent stages. To this aim, varactor-tuned lossy resonators are employed in its complementary-diplexer networks in order to incorporate the aforementioned spectrally-adaptive capabilities in terms of center frequencies and type of group-delay profile for the two NGD bands.

For this prototype, a Rogers 4003C substrate with the following parameters was used for fabrication: relative dielectric permittivity $\varepsilon_r = 3.38$, dielectric thickness $H = 1.524$ mm, metal thickness $t = 17.8$ μm, and dielectric loss tangent $\tan(\delta_D) = 0.0027$. Varactor diodes model SMV1234 from Skyworks (capacitance tuning range of 1.32–9.63 pF) were employed as electronic-tuning elements, and SMD 450-Ω resistors were incorporated in the resonators to implement

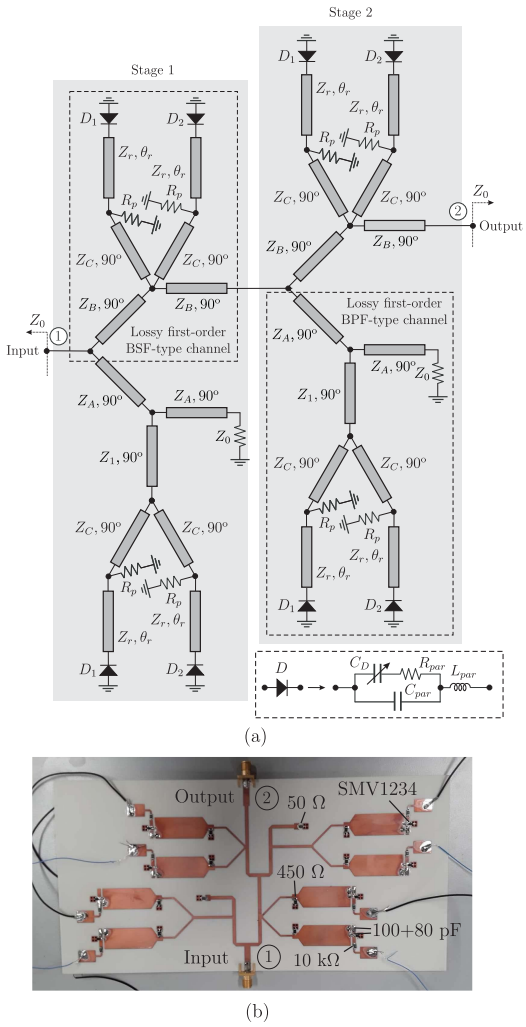

Fig. 14. Manufactured microstrip prototype of input-reflectionless dual-band NGD circuit based on the in-series cascade of two Type-I dual-band first-order NGD stages. (a) Ideal circuit schematic ($Z_0 = 50\ \Omega$, $f_d = 2$ GHz: $Z_A = Z_B = Z_1 = 7Z_0/5$, $Z_C = Z_A Z_B/Z_0$, $Z_r = 2Z_0/5$, $\theta_r(f_d) = 137^{\rm o}$, and $R_p = 9Z_0$; D_1 and D_2: varactor diodes replaced by their equivalent lumped-element model as provided in the datasheet). (b) Photograph.

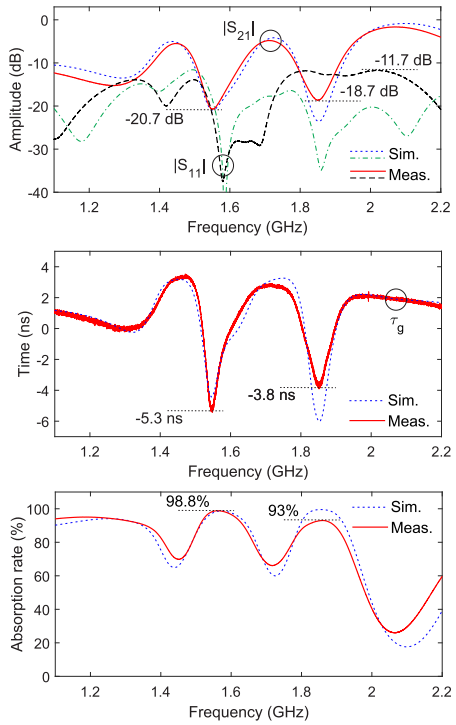

Fig. 15. Simulated and measured power transmission ($|S_{21}|$), input-reflection ($|S_{11}|$), and group-delay (τ_g) responses of the manufactured microstrip prototype of input-reflectionless dual-band NGD circuit for one tuned state, along with the corresponding simulated and measured power-absorption rates in percentage terms (i.e., $100 \times (1 - |S_{21}|^2 - |S_{11}|^2)$).

their appropriate conductance values. Besides, SMD 10-kΩ resistors and 180-pF capacitors (in-parallel 100-pF and 80-pF capacitors) were utilized in the biasing and DC-blocking networks of the varactors, respectively. The simulation and optimization of this circuits were performed with the software packages AWR Microwave Office and the measurements were carried out with a Keysight 5224A network analyzer.

A transmission-line implementation suitable for microstrip technology was selected for this reconfigurable dual-band NGD circuit. Specifically, the admittance inverters were realized as quarter-wavelength-at-2-GHz transmission-line segments and the lossy tunable resonating nodes as varactor-loaded half-wavelength transmission-line resonators being connected in parallel with resistors at their input nodes. Note that the variation range $[f_{min}, f_{max}]$ for the resonances of these varactor-tuned transmission-line resonators—which are ideally equal to the center frequencies of the NGD dual bands in the normalized lowpass frequency domain for the Type-I dual-band NGD stage—can be theoretically obtained from the following relationship:

$$C_{min} \leq \left| \frac{\tan\left(\frac{f_{max}}{f_d}\theta_r(f_d)\right)}{2\pi\, Z_r\, f_{max}} \right| < \left| \frac{\tan\left(\frac{f_{min}}{f_d}\theta_r(f_d)\right)}{2\pi\, Z_r\, f_{min}} \right| \leq C_{max} \tag{16}$$

where $[C_{min}, C_{max}]$ is the capacitance-variation range of the varactors, and Z_r and $\theta_r(f_d)$ are the characteristic impedance and electrical length at the design frequency $f_d = 2$ GHz, respectively, of the transmission-line segment of the resonators. Hence, to have a variation of the resonances in these resonators in the interval 1.5–2 GHz for the selected values $Z_r = 50\ \Omega$ and $\theta_r(f_d) = 137^{\rm o}$, it turns out from (16) that $C_{min} \leq 1.48$ pF and $C_{max} \geq 9.38$ pF—which is fulfilled by the selected varactor model. Nevertheless, when considering real varactors—which usually provide wider capacitance-variation ranges—and the frequency dependence of the transmission-line admittance inverters and other practical effects, the tuning range in center frequency for the NGD dual bands can be enlarged—as it will be the case for this prototype that will tune in a broader measured frequency range. The values for the design parameters were obtained by means of common microwave-filter-realization techniques from its coupling-routing diagram after some optimization to compensate the effects not contemplated by it, such as the frequency dependence of the transmission-line-based admittance inverters. Moreover, in the practical implementation, the loss effect of the varactors—i.e., loss resistance R_{par} that was estimated about 1.2 Ω at the 2-GHz design frequency—and the cumulative effects of the substrate conductor and

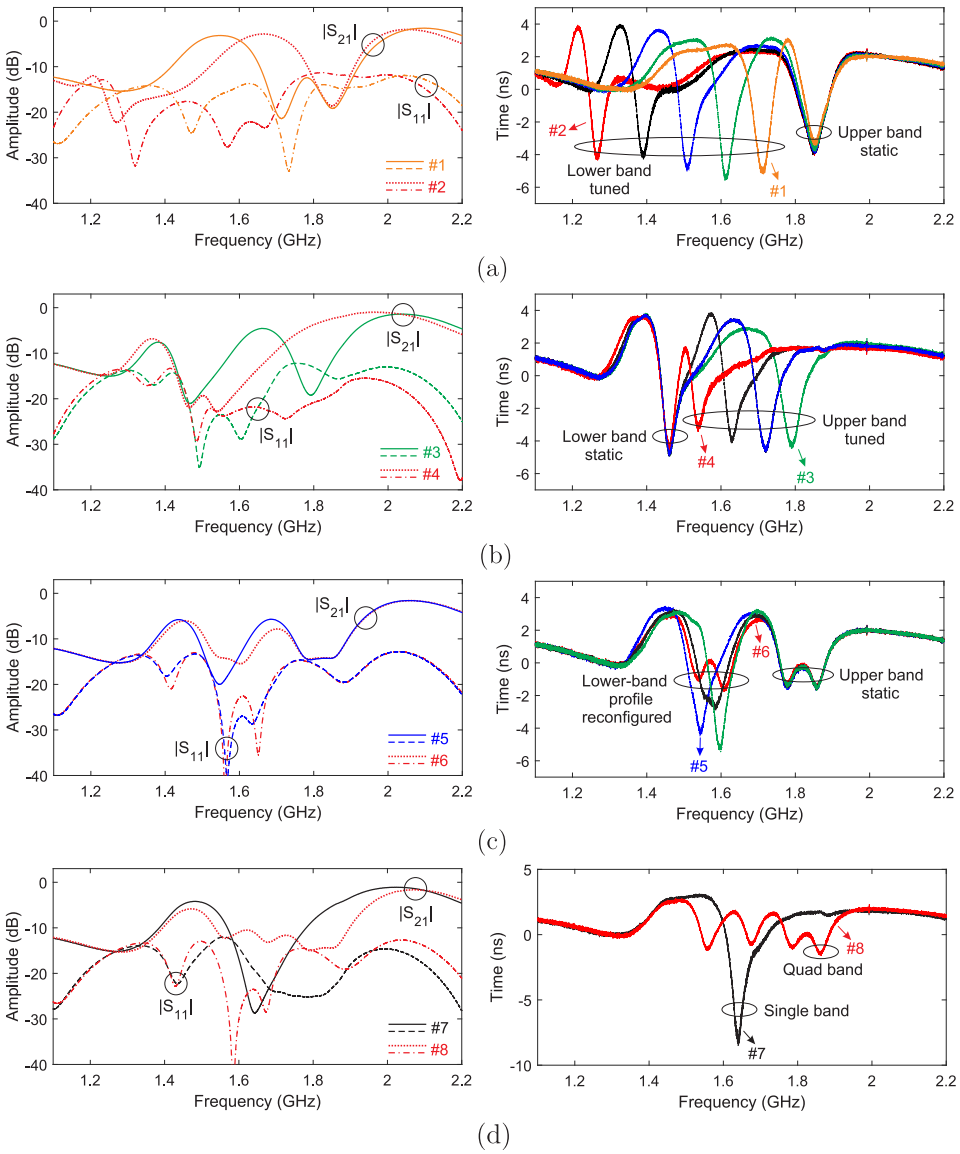

Fig. 16. Measured reconfiguration capabilities of the manufactured microstrip prototype of input-reflectionless dual-band NGD circuit in terms of group-delay (τ_g) response and measured power transmission ($|S_{21}|$) and input-reflection ($|S_{11}|$) responses for some example tuned states (referred to as #1, #2, . . . , #8). (a) Center-frequency tuning of the lower band when the upper one remains static for the same type of group-delay profile (maximum-NGD response). (b) Center-frequency tuning of the upper band when the lower one remains static for the same type of group-delay profile (maximum-NGD response). (c) Reconfiguration of the type of NGD profile of the lower band (maximum-NGD, quasi-flattened-NGD, and quasi-equi-ripple-NGD responses) when the upper one remains static with quasi-equi-ripple NGD shape. (d) Single-band maximum-NGD and quad-band states.

dielectric loss were taken into account when selecting the values for the in-parallel resistors $R_p = 450\ \Omega$ in order to obtain the desired NGD depths and bandwidths according to the theoretical analysis given in Section II. The parasitic inductance of the varactors $L_{par} = 0.45$ nF was compensated by shortening the length of the associated transmission-line segments of the resonators. The ideal circuit schematic, along with the equivalent lumped-element model of the varactor diode, and a photograph of the developed microstrip prototype are shown in Fig. 14.

The simulated and measured power transmission and group-delay responses of the manufactured microstrip prototype of input-reflectionless dual-band NGD circuit for one tuned state are compared in Fig. 15. As can be seen, despite the sensitivity of this type of RF circuit to loss effects, a reasonable agreement between predicted and experimental results is obtained so that the RF design principle is verified. Note that, when compared to the theoretical expectations as illustrated by the various examples of ideal responses provided in Section II, some performance discrepancies—mainly in terms of deteriorated amplitude flatness in the passband regions—is observed. This is attributed to the frequency-dependent behavior of the transmission-line-based admittance inverters, which is not considered by the coupling-routing-diagram formalism [43]– [45]. Furthermore, although to a less extent, the frequency dependence of some loss effects—e.g., conductor and dielectric losses of the microstrip substrate—or the specific frequency-variation profiles of the varactor-loaded transmission-line resonators—which are neither considered by the coupling-routing-diagram analytical framework—have also

TABLE I
COMPARISON WITH PRIOR-ART RECONFIGURABLE RF PASSIVE NGD CIRCUITS

	[36]	[38]	[39]	[40]	This work
Circuit structure and technology	Microstrip coupler in reflective mode loaded with varactors	Microstrip-lossy-resonator-loaded stub with varactors	Microstrip transversal network with varactor-tuned lossy resonators	Microstrip couplers in balanced-circuit architecture with varactors	Microstrip complementary diplexer with varactor-loaded lossy resonators
Number of bands	1	1	1	1	2 (scalable to any number)
Frequency control	×	×	✓	×	✓
NGD-shape/ bandwidth control	✓ (with two in-series-cascaded stages)	Partial (not equi-ripple/ flattened states)	Partial (not absolute-bandwidth control)	Partial (not equi-ripple/ flattened states)	✓ (through multi-NGD-band merging)
Multi-functionality co-integration	×	×	×	×	✓ (UWB filter and directional coupler)
Reflectionless behavior	Two-port-type	Two-port-type	Two-port-type	Two-port-type	✓ Input-type (valid for two-port-type)
Performance metrics: f_0 (GHz)/τ_{g0} (ns)/ $\Delta_{\text{NGD}}(\%)/L_0$ (dB)	Fig. 7: 2.14/−2 to −10/ 2.1/23.2 to 36 Fig. 9: 2.13/−2.2 to −7/ 6.1/45.2 to 60.4	Figs. 3–5: 1/−0.2 to −1.9/ N.A./2.5 to 3.4	Fig. 4: 2.02 to 2/ −0.67 to −0.92/ 2.7 to 3/2.92 to 3.25	Fig. 11(a) and (b): 1.15/−0.8 to −2/ N.A./22.5 to 26.8 Fig. 12(a) and (b): 1.15/0 to −90/ N.A./14 to 53	#1: 1.71/−5/4.1/21.4 (lower) 1.85/−3.3/4.2/19.2 (upper) #2: 1.26/−4.2/4.5/22.3 (lower) 1.85/−3.8/5.2/18.6 (upper) #3: 1.46/−4.7/6.3/21 (lower) 1.79/−4.3/4.7/19.2 (upper) #4: 1.46/−4.4/3.6/21.9 (lower) 1.54/−3.1/5.6/22.8 (upper) #7: 1.64/−8.1/7.3/28.7 (merged)
Effective area ($\times\lambda_g^2$)	N.A.	N.A.	N.A.	0.44×0.19	0.63×1.43 (at 1.26 GHz)

$f_0, \tau_{g0}, \Delta_{\text{NGD}}$, and L_0: center frequency of the NGD band, NGD value at f_0, relative-to-f_0 NGD bandwidth, and power-insertion-loss level at f_0, respectively (in [36] and [38]–[40], the relevant figures associated to the provided data are indicated). λ_g: guided wavelength at the center frequency (lower tunable center frequency in frequency-adaptive NGD circuits). #1, #2, #3, #4, and #7: examples of tuned states in Fig. 16(a), (b), and (d) of this work. N.A.: not available.

some influence on this disagreement. The main measured performance metrics for the lower and upper NGD bands, respectively, are as follows: center frequencies of 1.55 GHz and 1.85 GHz, NGD bandwidths equal to 82 MHz and 93 MHz, NGD values at the center frequencies equal to −5.3 ns and −3.8 ns, insertion-loss levels at the center frequencies of 20.7 dB and 18.7 dB, and input-power-matching levels higher than 11.7 dB in the spectral range 1.1–2.2 GHz. In Fig. 15, the simulated and measured power-absorption rates in percentage terms corresponding to this tuned state are also included. They reveal measured power-absorption rates at the NGD depths of the lower and upper NGD bands of 98.8% and 93%—when compared to the simulated values of 98.7% and 99.5%—, respectively, as further practical confirmation of the input-absorptive/reflectionless nature of the built prototype.

The measured tuning capabilities of this microstrip prototype in terms of group-delay response, along with the measured power transmission and input-reflection responses for some example tuned states, are illustrated in Fig. 16. Note that, in all cases, the varactors in the peer lossy resonators of the BSF-based and BPF-based channels of the complementary diplexer of each stage must be synchronously adjusted to preserve the input-reflectionless behavior, leading to input-power-matching levels higher than 11.4 dB in the represented frequency range for all these measured states. In particular, Fig. 16(a) shows how the lower NGD band can be tuned in center frequency in the range 1.26–1.72 GHz (NGD depth in the interval 4.2–5.3 ns) when the upper one remains static in frequency at 1.85 GHz (NGD depth in the range 3.2–3.8 ns) for the same type of maximum-NGD profile. Analogous results in terms of upper-band tuning in the range of 1.54–1.79-GHz (NGD depth in the interval 3.2–4.4 ns) when the upper band is spectrally fixed at 1.46 GHz (NGD depth in the range 4.4–4.7 ns) are provided in Fig. 16(b). In Fig. 16(c), for a static upper band with quasi-equi-ripple-NGD profile, it is verified how the lower band can be reconfigured in shape to exhibit maximum-NGD, quasi-flattened-NGD, and quasi-equi-ripple-NGD shapes as a demonstration of flexible NGD patterning. Finally, Fig. 16(d) represents two illustrative quad-band (center frequencies of 1.56 GHz, 1.68 GHz, 1.79 GHz, and 1.86 GHz with NGD depths of 1.1 ns, 0.75 ns, 0.95 ns, and 1.4 ns, respectively) and single-band (center frequency of 1.64 GHz and NGD depth of 8 ns) NGD states. They were respectively set by tuning apart and merging together the NGD bands associated to the four lossy resonators in the BPF channels corresponding to the two complementary-diplexer stages.

Finally, Table I provides a comparison of the developed tunable microstrip prototype of input-reflectionless dual-band NGD circuit with some prior-art approaches of reconfigurable RF passive NGD circuits. As can be seen, whereas the devices in [36] and [40] can feature more-negative NGD values but at the expense of much-higher insertion-loss levels, the circuit of this work is the one showing more spectrally-adaptive capabilities for multi-band NGD responses. Furthermore, its potential for co-integration with other RF-analog-signal-processing functionalities has been theoretically proven—i.e., UWB filter and directional coupler with embedded NGD bands in Section II.E—, unlike in the past works in [36] and [38]– [40].

IV. CONCLUSION

Low-reflection frequency-reconfigurable multi-band NGD circuit networks based on two different approaches have been reported. Both of them make use of tunable lossy-complementary-diplexer architectures in their basic first-order

stages to realize input-reflectionless spectrally-adaptive multi-band NGD RF-analog-processing actions. Furthermore, their extension to higher-order, in-series-cascade, and symmetrical architectures, as well as to RF multi-functional components with embedded multi-band NGD actions, has been also illustrated. As a result, one/two-port-reflectionless multi-band NGD actions with broader operational ranges and sharper group-delay-region transitions, which can also be co-integrated with other RF functionalities, can be performed. For practical-validation purposes, a varactor-tuned input-reflectionless microstrip prototype has been developed and tested. It consists of a two-stage-in-series-cascade dual-band NGD circuit, which has successfully verified the proposed RF design principles. Note finally that, although here applied to an electronically-reconfigurable RF transmission-line implementation, the presented study to design adaptive multi-band NGD analog-signal processors is general for any technology and frequency range.

REFERENCES

[1] C. Caloz, S. Gupta, Q. Zhang, and B. Nikfal, "Analog signal processing: A possible alternative or complement to dominantly digital radio schemes," *IEEE Microw. Mag.*, vol. 14, no. 6, pp. 87–103, Sep./Oct. 2013.

[2] B. Ravelo, *Negative Group Delay Devices: From Concepts to Applications*. Stevenage, U.K.: Institution Engineering and Technology, 2019.

[3] B. Ravelo, M. L. Roy, and A. Pérennec, "Application of negative group delay active circuits to the design of broadband and constant phase shifters," *Microw. Opt. Technol. Lett.*, vol. 50, no. 12, pp. 3078–3080, Dec. 2008.

[4] L. He, W. Li, J. Hu, and Y. Xu, "A 24-GHz source-degenerated tunable delay shifter with negative group delay compensation," *IEEE Microw. Wireless Compon. Lett.*, vol. 28, no. 8, pp. 687–689, Aug. 2018.

[5] K.-P. Ahn, R. Ishikawa, and K. Honjo, "Group delay equalized UWB InGaP/GaAs HBT MMIC amplifier using negative group delay circuits," *IEEE Trans. Microw. Theory Techn.*, vol. 57, no. 9, pp. 2139–2147, Sep. 2009.

[6] S. K. Podilchak, B. M. Frank, A. P. Freundorfer, and Y. M. M. Antar, "High speed metamaterial-inspired negative group delay circuits in CMOS for delay equalization," in *Proc. 2nd Microsyst. Nanoelectron. Res. Conf.*, Ottawa, ON, Canada, Oct. 2009, pp. 9–12.

[7] H. Noto, K. Yamauchi, M. Nakayama, and Y. Isota, "Negative group delay circuit for feed-forward amplifier," in *IEEE MTT-S Int. Microw. Symp. Dig.*, Honolulu, HI, USA, Jun. 2007, pp. 1103–1106.

[8] H. Choi, Y. Jeong, C. D. Kim, and J. S. Kenney, "Efficiency enhancement of feedforward amplifiers by employing a negative group-delay circuit," *IEEE Trans. Microw. Theory Techn.*, vol. 58, no. 5, pp. 1116–1125, May 2010.

[9] H. Choi, G. Chaudhary, T. Moon, Y. Jeong, J. Lim, and C. D. Kim, "A design of composite negative group delay circuit with lower signal attenuation for performance improvement of power amplifier linearization techniques," in *IEEE MTT-S Int. Microw. Symp. Dig.*, Baltimore, MD, USA, Jun. 2011, pp. 1–4.

[10] A. Taslimi, W. Alomar, and A. Mortazawi, "Phase compensated serially fed array using the antenna as a part of negative group delay circuit," in *IEEE MTT-S Int. Microw. Symp. Dig.*, Phoenix, AZ, USA, May 2015, pp. 1–4.

[11] H. Mirzaei and G. V. Eleftheriades, "Arbitrary-angle squint-free beamforming in series-fed antenna arrays using non-Foster elements synthesized by negative-group-delay networks," *IEEE Trans. Antennas Propag.*, vol. 63, no. 5, pp. 1997–2010, May 2015.

[12] H. Mirzaei and G. V. Eleftheriades, "Realizing non-Foster reactive elements using negative-group-delay networks," *IEEE Trans. Microw. Theory Techn.*, vol. 61, no. 12, pp. 4322–4332, Dec. 2013.

[13] S. Kolev, B. Delacressonniere, and J.-L. Gautier, "Using a negative capacitance to increase the tuning range of a varactor diode in MMIC technology," *IEEE Trans. Microw. Theory Techn.*, vol. 49, no. 12, pp. 2425–2430, Dec. 2001.

[14] M. Zhu and C.-T. M. Wu, "A tunable non-foster T-network loaded transmission line using distributed amplifier-based reconfigurable negative group delay circuit," in *Proc. Asia–Pacific Microw. Conf. (APMC)*, Kyoto, Japan, Nov. 2018, pp. 720–722.

[15] T. Zhang and T. Yang, "A novel fully reconfigurable non Foster capacitance using distributed negative group delay networks," *IEEE Access*, vol. 7, pp. 92768–92777, 2019.

[16] B. Ravelo, A. Pérennec, and M. L. Roy, "Synthesis of broadband negative group delay active circuits," in *IEEE MTT-S Int. Microw. Symp. Dig.*, Honolulu, HI, USA, Jun. 2007, pp. 2177–2180.

[17] B. Ravelo, A. Pérennec, M. L. Roy, and Y. G. Boucher, "Active microwave circuit with negative group delay," *IEEE Microw. Wireless Compon. Lett.*, vol. 17, no. 12, pp. 861–863, Dec. 2007.

[18] M. Kandic and G. E. Bridges, "Asymptotic limits of negative group delay in active resonator-based distributed circuits," *IEEE Trans. Circuits Syst. I, Reg. Papers*, vol. 58, no. 8, pp. 1727–1735, Aug. 2011.

[19] C.-T.-M. Wu and T. Itoh, "Maximally flat negative group-delay circuit: A microwave transversal filter approach," *IEEE Trans. Microw. Theory Techn.*, vol. 62, no. 6, pp. 1330–1342, Jun. 2014.

[20] R. Das, Q. Zhang, and H. Liu, "Lossy coupling matrix synthesis approach for the realization of negative group delay response," *IEEE Access*, vol. 6, pp. 1916–1926, 2018.

[21] B. Mini-Circuits, "Reflectionless filters improve linearity and dynamic range," *Microw. J.*, vol. 58, no. 8, pp. 42–50, Aug. 2015.

[22] D. Psychogiou and R. Gomez-Garcia, "Reflectionless adaptive RF filters: Bandpass, bandstop, and cascade designs," *IEEE Trans. Microw. Theory Techn.*, vol. 65, no. 11, pp. 4593–4605, Nov. 2017.

[23] M. D. Hickle and D. Peroulis, "Theory and design of frequency-tunable absorptive bandstop filters," *IEEE Trans. Circuits Syst. I, Reg. Papers*, vol. 65, no. 6, pp. 1862–1874, Jun. 2018.

[24] M. A. Morgan, "Think outside the band: Design and miniaturization of absorptive filters," *IEEE Microw. Mag.*, vol. 19, no. 7, pp. 54–62, Nov. 2018.

[25] R. Gómez-García, D. Psychogiou, J.-M. Muñoz-Ferreras, and L. Yang, "Avoiding RF isolators: Reflectionless microwave bandpass filtering components for advanced RF front ends," *IEEE Microw. Mag.*, vol. 21, no. 12, pp. 68–86, Dec. 2020.

[26] M. A. Morgan, W. M. Groves, and T. A. Boyd, "Reflectionless filter topologies supporting arbitrary low-pass ladder prototypes," *IEEE Trans. Circuits Syst. I, Reg. Papers*, vol. 66, no. 2, pp. 594–604, Feb. 2019.

[27] A. Guilabert, M. A. Morgan, and T. A. Boyd, "Reflectionless filters for generalized elliptic transmission functions," *IEEE Trans. Circuits Syst. I, Reg. Papers*, vol. 66, no. 12, pp. 4606–4618, Dec. 2019.

[28] G. Chaudhary, Y. Jeong, and J. Lim, "Microstrip line negative group delay filters for microwave circuits," *IEEE Trans. Microw. Theory Techn.*, vol. 62, no. 2, pp. 234–243, Feb. 2014.

[29] B. Ravelo, "Theory of coupled line coupler-based negative group delay microwave circuit," *IEEE Trans. Microw. Theory Techn.*, vol. 64, no. 11, pp. 3604–3611, Nov. 2016.

[30] M. A. Sánchez-Soriano, J. Dura, S. Sirci, and S. Marini, "Signal-interference-based structure with negative group delay properties," in *Proc. 48th Eur. Microw. Conf. (EuMC)*, Madrid, Spain, Sep. 2018, pp. 1021–1024.

[31] L.-F. Qiu, L.-S. Wu, W.-Y. Yin, and J.-F. Mao, "Absorptive bandstop filter with prescribed negative group delay and bandwidth," *IEEE Microw. Wireless Compon. Lett.*, vol. 27, no. 7, pp. 639–641, Jul. 2017.

[32] A. Goel, B. Analui, and H. Hashemi, "Tunable duplexer with passive feed-forward cancellation to improve the RX-TX isolation," *IEEE Trans. Circuits Syst. I, Reg. Papers*, vol. 62, no. 2, pp. 536–544, Feb. 2015.

[33] L. Gao, T.-W. Lin, and G. M. Rebeiz, "Design of tunable multi-pole multi-zero bandpass filters and diplexer with high selectivity and isolation," *IEEE Trans. Circuits Syst. I, Reg. Papers*, vol. 66, no. 10, pp. 3831–3842, Oct. 2019.

[34] A. Zakharov and M. Ilchenko, "Circuit function characterizing tunability of resonators," *IEEE Trans. Circuits Syst. I, Reg. Papers*, vol. 67, no. 1, pp. 98–107, Jan. 2020.

[35] G. Zhang, S. Liu, W. Chen, Z. Zhang, and J. Yang, "Design method for compact multifunctional reconfigurable filtering power divider on a new tunable three-port multi-mode topology," *IEEE Trans. Circuits Syst. I, Reg. Papers*, vol. 67, no. 12, pp. 4580–4592, Dec. 2020.

[36] G. Chaudhary, Y. Jeong, and J. Im, "A design of reconfigurable negative group delay circuit without external resonators," *IEEE Antennas Wireless Propag. Lett.*, vol. 14, pp. 883–886, Dec. 2014.

[37] T. Zhang, R. Xu, and C.-T.-M. Wu, "Voltage-insensitive negative group delay circuit based on a stepped-impedance distributed amplifier," *IEEE Microw. Wireless Compon. Lett.*, vol. 27, no. 11, pp. 1007–1009, Nov. 2017.

[38] L.-S. Wu, L.-F. Qiu, and J.-F. Mao, "A negative group delay tuner with stable insertion loss," in *IEEE MTT-S Int. Microw. Symp. Dig.*, Honolulu, HI, USA, Jun. 2017, pp. 473–475.

[39] G. Chaudhary and Y. Jeong, "Tunable center frequency negative group delay filter using coupling matrix approach," *IEEE Microw. Wireless Compon. Lett.*, vol. 27, no. 1, pp. 37–39, Jan. 2017.
[40] T. Zhang, T. Yang, and P.-L. Chi, "Novel reconfigurable negative group delay circuits with independent group delay and transmission loss/gain control," *IEEE Trans. Microw. Theory Techn.*, vol. 68, no. 4, pp. 1293–1303, Apr. 2020.
[41] B. Ravelo, "Innovative theory on multiband NGD topology based on feedback-loop power combiner," *IEEE Trans. Circuits Syst. II, Exp. Briefs*, vol. 63, no. 8, pp. 738–742, Aug. 2016.
[42] R. Gómez-García, J.-M. Muñoz-Ferreras, W. Feng, and D. Psychogiou, "Input-reflectionless negative-group-delay bandstop-filter networks based on lossy complementary duplexers," in *IEEE MTT-S Int. Microw. Symp. Dig.*, Boston, MA, USA, Jun. 2019, pp. 1–4.
[43] A. Atia, A. Williams, and R. Newcomb, "Narrow-band multiple-coupled cavity synthesis," *IEEE Trans. Circuits Syst.*, vol. CAS-21, no. 5, pp. 649–655, Sep. 1974.
[44] R.-J. Cameron, C.-M. Kudsia, and R. R. Mansour, *Microwave Filters for Communication Systems: Fundamentals, Design, and Applications*, 1st ed. New York, NY, USA: Wiley, 2007.
[45] J.-S. Hong, *Microstrip Filters for RF/Microwave Applications*, 2nd ed. New York, NY, USA: Wiley, 2011.
[46] R. Gómez-García, J.-M. Muñoz-Ferreras, and D. Psychogiou, "High-order input-reflectionless bandpass/bandstop filters and multiplexers," *IEEE Trans. Microw. Theory Techn.*, vol. 67, no. 9, pp. 3683–3695, Sep. 2019.

Roberto Gómez-García (Senior Member, IEEE) received the Dipl.-Eng. degree in telecommunication engineering and the Ph.D. degree in electrical and electronic engineering from the Polytechnic University of Madrid, Madrid, in 2001 and 2006, respectively.

Since 2006, he has been an Associate Professor with the Department of Signal Theory and Communications, University of Alcalá, Alcalá de Henares, Spain. He has been, for several research stays, with the C2S2 Department, XLIM Research Institute, University of Limoges, Limoges, France, the Telecommunications Institute, University of Aveiro, Aveiro, Portugal, the U.S. Naval Research Laboratory, Microwave Technology Branch, Washington, DC, USA, and Purdue University, West Lafayette, IN, USA. He had been an Invited Professor with the Gdansk University of Technology, Poland, from 2019 to 2020. He is currently an Adjunct Part-Time Professor with the University of Electronic Science and Technology of China, Chengdu, China. His current research interests include the design of fixed/tunable high-frequency filters and multiplexers in planar, hybrid, and monolithic microwave-integrated circuit technologies, multifunction circuits and systems, and software-defined radio and radar architectures for telecommunications, remote sensing, and biomedical applications. In these topics, he has authored/coauthored about 110 articles in international journals and 150 papers in international conferences. He also serves as a member for the Technical Review Board for several IEEE and EuMA conferences. He is also a member of the IEEE MTT-S Filters (MTT-5), the IEEE MTT-S RF MEMS and Microwave Acoustics (MTT-6), the IEEE MTT-S Wireless Communications (MTT-23), the IEEE MTT-S Biological Effects and Medical Applications of RF and Microwave (MTT-28), and the IEEE CAS-S Analog Signal Processing Technical Committees. He was a recipient of the 2016 IEEE Microwave Theory and Techniques Society (MTT-S) Outstanding Young Engineer Award. He has also been an IEEE CAS-S Distinguished Lecturer since 2020. He was an Associate Editor of the IEEE TRANSACTIONS ON MICROWAVE THEORY AND TECHNIQUES from 2012 to 2016 and the IEEE TRANSACTIONS ON CIRCUITS AND SYSTEMS—I: REGULAR PAPERS from 2012 to 2015. He was a Senior Editor of the IEEE JOURNAL ON EMERGING AND SELECTED TOPICS IN CIRCUITS AND SYSTEMS from 2016 to 2017. He was a Guest Editor of several special/focus issues and sections in IEEE and IET journals. He is also an Associate Editor of the IEEE MICROWAVE AND WIRELESS COMPONENTS LETTERS, IEEE JOURNAL OF ELECTROMAGNETICS, RF AND MICROWAVES IN MEDICINE AND BIOLOGY, IEEE ACCESS, *IET Microwaves, Antennas & Propagation*, and the *International Journal of Microwave and Wireless Technologies*, a TC-5 Topic Editor of IEEE JOURNAL OF MICROWAVES, and the MTT-S Newsletter Working Group Chair.

José-María Muñoz-Ferreras (Member, IEEE) received the degree in telecommunication engineering and the Ph.D. degree in electrical and electronic engineering from the Polytechnic University of Madrid, Spain, in 2004 and 2008, respectively.

He is currently an Associate Professor with the Department of Signal Theory and Communications, University of Alcalá, Alcalá de Henares, Spain. His current research interests include radar signal processing, advanced radar systems and concepts, and microwave/RF circuits and systems, specifically focusing on high-resolution inverse synthetic aperture radar images, and the design and validation of radar systems for short-range applications. He is also a member of the IEEE MTT-S Biological Effects and Medical Applications of RF and Microwave (MTT-28) Technical Committee and a reviewer of several IEEE and IET publications. He also serves as a member of the Technical Review Board for the IEEE International Geoscience and Remote Sensing Symposium, the IEEE Radar Conference, the European Radar Conference, and the IEEE MTT-S International Microwave Symposium.

Dimitra Psychogiou (Senior Member, IEEE) received the Dipl.-Eng. degree in electrical and computer engineering from the University of Patras, Patras, Greece, in 2008, and the Ph.D. degree in electrical engineering from the Swiss Federal Institute of Technology (ETH), Zürich, Switzerland, in 2013.

She is currently a Professor of electrical and electronic engineering with the University College Cork (UCC) and the Tyndall National Institute, Cork, Ireland. Prior to joining UCC, she was a Senior Research Scientist with Purdue University, West Lafayette, IN, USA, and an Assistant Professor with the University of Colorado Boulder, Boulder, CO, USA. Her current research interests include RF design and characterization of reconfigurable microwave and millimeter-wave passive components, RF MEMS, acoustic wave resonator-based filters, tunable filter synthesis, and frequency-agile antennas. Her research has been presented in more than 160 IEEE publications. She is also a Senior Member of URSI and a member of the IEEE MTT-S Filters and Passive Components (MTT-5) and Microwave Control Materials and Devices (MTT-13) committees. Furthermore, she serves on the Technical Review Board for various IEEE and EuMA conferences and journals. She received the 2020 CAREER Award from the National Science Foundation (NSF), the 2020 URSI Young Scientist Award, and the Junior Faculty Outstanding Research Award from UC Boulder. She is also the Chair of MMT-13 and the Secretary of USNC-URSI Commission D. She is also an Associate Editor of the IEEE MICROWAVE AND WIRELESS COMPONENTS LETTERS and the *International Journal of Microwave and Wireless Technologies*. Previously, she was an Associate Editor of the *IET Microwaves, Antennas & Propagation* journal.